Global propagation of body waves revealed by cross-correlation analysis of seismic hum

K. Nishida[1]

Seismic interferometry has now been applied to the exploration of the Earth's interior at scales ranging from local to global. Most studies have used surface-wave propagation. Recently, some studies have focused on body-wave propagation on local and regional scales but not on a global scale. In this study, we succeed in extracting global body-wave propagation (of P, PP, PKP, S, SS, ScS, $P'P'$, etc. waves) using seismic hum with wavenumber–frequency filtering in the range of 5 to 40 mHz. Although the observed body-wave propagation is similar to that of the corresponding components of Green's functions, there are two differences between them: the lack of reflection phases in the observation and the dominance of shear-coupled PL waves in the observation. These differences originate from the dominance of shear-traction sources on the Earth's surface, which causes the breakdown of equipartition among modes with different radial orders. For further studies of body-wave exploration by seismic interferometry, these differences should be considered.

1. Introduction

Seismic interferometry [e.g., Curtis *et al.*, 2006] is an approach that can be used to extract the elastic response between two stations by cross-correlating a random wavefield. Shapiro *et al.* [2005] performed a cross-correlation analysis of long sequences of ambient seismic noise at around 0.1 Hz to obtain a group-velocity map of Rayleigh waves in southern California. This method has now been applied at scales ranging from local and regional [e.g., Ritzwoller *et al.*, 2011] to global [Nishida *et al.*, 2009]. Most studies have focused on surface-wave propagation, although the calculated cross-correlation functions (CCFs) of a random wavefield contain not only surface waves but also body waves. Surface-wave tomography has fine lateral resolution, but it has inherently poor vertical resolution in the deep structure. Body-wave exploration offers a better vertical resolution of the deep Earth's structure than surface-wave exploration.

Recently, body-wave propagation on local and regional scales has been extracted by using seismic interferometry. There have been two types of studies. One is body-wave extraction using ambient noise: reflection phases on a 1-km scale [Draganov *et al.*, 2007], direct P waves on a 10-km scale [Roux, 2005], and reflection phases at the Moho, 440- and 660-km discontinuities on a 500-km scale [Poli *et al.*, 2012a, b]. The other type uses seismic coda [e.g., Tonegawa

et al., 2009]: direct and reflection phases on a 100-km scale. However, there is still no study on a global scale.

For the detection of the global propagation of seismic waves, low-frequency seismic data are effective [Nishida *et al.*, 2009] because of their long wavelength. For the extraction of global body-wave propagation, we conducted a cross-correlation analysis of the background seismic wavefield from 5 to 40 mHz, now known as seismic hum [e.g., Nishida, 2013]

2. Data

We analyzed continuous sampling records in a time period from 2004 to 2011 at 658 stations with three components of broadband seismometers (STS-1, STS2, and STS2.5) at the lowest ground noise levels (Figure 1(a)). We used data obtained from the stations of the International Federation of Digital Seismographic Networks (FSDN) and F-net stations of the National Research Institute for Earth Science and Disaster Prevention (NIED). For each station, the complete record was divided into about 2.8-h segments with an overlap of 1.4 h. To avoid effects from earthquakes, we discarded all the seismically disturbed segments [Nishida and Kobayashi, 1999] using the global CMT catalog [Ekström *et al.*, 2012]. We calculated cross spectra between every pair of different stations for their common record segments at periods from 5 to 40 mHz for 9 years. We did not use the cross spectra when the horizontal components of their amplitudes were 200 times greater than in Peterson's New Low Noise Model (NLNM) [Peterson, 1993] and when the vertical components of their amplitudes were 40 times greater than in NLNM. We stacked real parts of the cross spectra between transverse (TT), radial (RR), and vertical (ZZ) components for 9 years. Here, we define radial and transverse components for each station pair. Figure 1(b) shows a histogram showing the distribution of receiver-receiver ranges for the CCFs

To remove the effects of source time functions, we normalized the cross spectra by the power spectrum of NLNM. This is because the Green's function (i.e., the impulse response) can be retrieved from the normalized cross spectra [Nakahara, 2006]. We did not normalized cross spectra by power spectra of observed ground motions but by that of NLNM for the following reasons: (1) Normalization by power spectra of the random elastic wavefield is better. However, power spectra of observed ground motions at stations include the random elastic wavefield and site-dependent noise. Because the amplitudes of site-dependent noise are higher than those of the random wavefield in most cases, the separation is difficult. High variabilities of the noise biases the results of the normalization. (2) Nishida *et al.* [2002] showed that power spectra of the random wavefield at stations can be approximated by that of NLNM in this frequency range. (3) Although the normalization by NLNM is ad hoc, the procedure is stable and simple.

[1]Earthquake Research Institute, University of Tokyo, 1-1-1 Yayoi 1, Bunkyo-ku, Tokyo 113-0032, Japan (knishida@eri.u-tokyo.ac.jp)

3. Frequency–wavenumber spectra

To detect body-wave propagation in the frequency–wavenumber (FK) domain, we calculated FK spectra for the cross spectra as follows. By assuming homogeneous and isotropic excitation of the Earth's normal modes, the TT, RR, and ZZ components of synthetic cross spectra (ϕ^{TT}, ϕ^{RR}, and ϕ^{ZZ}) can be represented by a superimposition of associate Legendre functions $P_{lm}(\cos\Theta)$ as a function of separation distance Θ [Nishida *et al.*, 2002; Nishida *et al.*, 2008a] as

$$\phi^{TT}(\Theta) = -\sum_l \left\{ \frac{c_l}{k^2} \frac{dP_{l1}}{d\Theta} + \frac{b_l}{k^2} \frac{P_{l1}}{\sin\Theta} \right\},$$

$$\phi^{RR}(\Theta) = -\sum_l \left\{ \frac{b_l}{k^2} \frac{dP_{l1}}{d\Theta} + \frac{c_l}{k^2} \frac{P_{l1}}{\sin\Theta} \right\}, \quad (1)$$

$$\phi^{ZZ}(\Theta) = \sum_l a_l P_{l0}, \quad (2)$$

where l is the angular order, k is the wavenumber $\sqrt{l(l+1)}$, and the coefficients a_l, b_l, and c_l represent normalized power spectral densities (PSDs) at frequency ω. This method is a natural extension of Aki's spatial autocorrelation method [Aki, 1957] from a flat case to spherical one. We estimated the coefficients a_l, b_l, and c_l by minimizing the square differences between the synthetic cross spectra and the observed ones.

A plot of a_l against the angular order l and frequency gives a FK spectrum of the ZZ component, that of b_l gives a FK spectrum of the RR component, and that of c_l gives a FK spectrum of the TT component as shown in Figure 2(a). The plots of the RR and ZZ components show clear fundamental spheroidal modes (Rayleigh waves), and that of the TT component shows fundamental toroidal modes (Love waves). The plots of the RR and ZZ components also show a clear physical branch of higher modes that corresponds to S- and SS-wave propagation. The phase velocity ranges from 7 to 8 km/s, which is comparable to typical Pn-wave velocity. This result suggests that the physical branch represents a crustal PL wave coupled with S and SS waves that are known, respectively, as a shear-coupled PL (SPL) wave and an SS coupled PL ($SSPL$) wave [Oliver, 1961; Baag and Langston, 1985]. The direct PL wave is a long-period wave train (30–50 s) in vertical and radial components beginning immediately after the P-wave arrival for epicentral distances less than $30°$. That is, it is a leaking spheroidal mode in the crust–mantle wave guide. For further discussion, we will identify the phases in the spatial–time domain, which are record sections of CCFs.

4. Global body-wave propagation in the spatial–time domain

For obtaining record sections of CCFs, we transformed the FK spectra to CCFs in the spatial–time domain. Before the transformation, we suppressed the FK spectra with phase velocity lower than those of fundamental toroidal or spheroidal modes. This procedure in the FK domain corresponds to stacking and phase velocity filtering in the spatial–time domain. If homogeneous and isotropic excitation is a stationary stochastic process, the display of the CCFs as a function of their separation distance should indicate seismic wave propagation. Hilbert transform of normalized CCFs can be regarded as the Green's function in the 2-D case: surface wave or boundary wave, whereas the time derivative in the 3-D case: body wave [e.g., Snieder, 2004; Nakahara, 2006]. Because the wavefield in our observation can be represented by superimposition of surface wave and body wave, the theoretical treatment is unclear. We took the Hilbert

transform of the CCFs for comparison with the corresponding components of the Green's functions, simply because the reconstruction is better than that by the time derivative.

Figure 3(a) shows the CCFs bandpass-filtered from 5 to 40 mHz every $0.2°$. The RR and ZZ components of the CCFs show propagating Rayleigh, P, S, and SS waves. We can also identify PP, PKP, and $P'P'$ waves. The TT component of the CCFs shows Love waves and S and ScS waves. Because the noise level of the horizontal components is higher than that of the vertical ones, phase identifications of RR and TT components are more difficult than those of the ZZ component.

These phase identifications suggest that the travel times can be approximated by those from Green functions. However, Forghani *et al.* [2010] pointed out that the body-wave amplitudes of the CCFs are underestimated compared to those predicted by the corresponding components of the Green's functions, when the random wavefield is excited by random surface sources. Incomplete source distribution leads to incomplete reconstruction of Green's functions.

5. Comparison with Green's functions

For a discussion on the difference between the observed CCFs and the corresponding components of the Green's functions, we calculated Green's functions for a spherical Earth model (PREM [Dziewonski and Anderson, 1981]) using a normal mode theory [Dahlen and Tromp, 1998]. For comparison, we bandpass-filtered the Green's functions from 5 to 40 mHz. Figure 3(b) shows the transverse components of the Green's functions due to a unit single force at the source in the transverse direction (TT), the radial components due to that in the radial direction (RR), and the vertical components due to that in the vertical direction (ZZ). Here, we normalized all the components of Green's functions by setting the P-wave amplitude of the Green's function (ZZ) at $80°$ equal to that of the CCF (ZZ). FK spectra of the Green's functions are also shown in Figure 2(b). We note that we kept the relative amplitudes of the Green's functions among the components.

The observed CCFs agree with the Green's functions, but we find three differences: (1) the dominant frequency of surface waves, (2) a lack of reflection phases in the CCFs, and (3) the dominance of SPL and $SSPL$ waves in the ZZ component of the CCFs.

First, high-frequency components of the surface waves of the CCFs are smaller than those of the Green's functions. For more detail, we show the ZZ component of the CCF and the Green's function at $80°$ in Figure 4(a). The CCF has the best signal-to-noise ratio because of the many pairs of cross spectra between stations in Japan and those in the USA (Figure 1(b)). We can find a difference in the dominant frequency of Rayleigh waves between them. The CCF includes many more low-frequency (≤ 10 mHz) surface waves than does the Green's function. The stacking procedure suppressed the high-frequency surface wave components, because of the large phase velocity anomalies resulting from lateral heterogeneities in the Earth's structure.

The second difference is the lack of reflection phases in the CCFs. We can identify only a weak SS wave in the TT component and weak PP, PPS, and SSS waves in the ZZ component, although the corresponding components of the Green's functions show clear ones. Geometrical spreading of the body waves and the small reflection coefficients affect the amplitudes of the reflection phases. For a proper reconstruction of the Green's function, the source must be at the appropriate stationary phase region that includes the Earth's

interior. Absence of the excitation sources in the Earth results in an underestimation of the extracted body-wave amplitudes [Forghani *et al.*, 2010]. This lack of reflection phases can be also interpreted as a breakdown of equipartition among modes with different radial orders [Snieder *et al.*, 2010] as a result of their source distribution being only on the Earth's surface [e.g., Nishida, 2013]. We note a good reconstruction of the ScS wave because the short separation distance reduces the amplitude loss resulting from geometrical spreading.

The third difference is the dominance of the SPL and $SSPL$ waves in the ZZ component of the CCFs. The CCFs in the ZZ component show propagation of the waves with a phase velocity from 7 to 8 km as shown in Figure 2(a), whereas the Green's functions (ZZ) lack them [Figure 2(b)]. We note that the both FK spectra of CCFs and Green's functions in RR components show dominance of SPL and $SSPL$ waves.

We now discuss the efficient excitation of an SPL wave. The excitation source of seismic hum can be represented by a random shear traction acting on a presumed sea-bottom horizon [Nishida *et al.*, 2008b]. The radiation patterns of P and S waves by surface shear traction are shown in Figure 4(b). The traction source radiates the strongest PL wave in the horizontal direction, as shown in the figure. The PL wave coupled with a mantle S wave (shear-coupled PL wave) becomes dominant. A schematic figure of the coupling mechanism is shown in Figure 4(b). If this mechanism works well, a direct PL wave should be also dominant. In fact, we can find a clear PL wave in the ZZ component of the CCFs [Figure 3(c)], whereas we cannot identify a PL wave in the ZZ components of the Green's function. The radiation pattern also explains the dominance of SPL waves of the Green's function in the RR components, because the single force acts in the horizontal direction.

6. Discussion

Here, we discuss two potential applications using the extracted body waves: (1) body-wave tomography and (2) inferring discontinuities such as those at 410 and 660 km.

The first application involves travel-time tomography using P- and S-wave arrivals. Although the stacked CCFs (Figure 4) show clear P- and S-wave arrivals, noise-to-signal ratios of individual CCFs are very low. The detection of a P-wave arrival for each CCF is quite difficult, and hence, we focus on S-wave measurements. Even picking the first arrival of the S-wave is difficult. In this case, travel-time measurement by using the cross-correlation method is realistic. For a measurement, we cannot separate the S waves from the SPL wave. The SPL wave biases the travel-time measurement because it is also sensitive to crustal P-wave structure. When we conduct the tomography, we must consider the appropriate sensitivity kernels for S and SPL waves.

The other application is inferring discontinuities (e.g., at 410 and 660 km) using upper and under reflection phases [e.g., Shearer and Masters, 1992]. For the detection of weak phases such as PP and SS precursors, the signal-to-noise ratio in this frequency range is too low. Hence, we must include higher frequency components of the CCFs for the detection [Poli *et al.*, 2012b]; however, global measurements at higher frequencies (>0.03 Hz) are beyond the scope of this study.

7. Conclusions

We succeeded in extracting body-wave propagation using seismic hum from 5 to 40 mHz by cross-correlating the background wavefield. The resultant CCFs show clear body-wave propagations (of P, PKP, S, SS, ScS, $P'P'$, etc. waves). Although the observed body-wave propagations are similar to those of the corresponding components of the Green's functions, there two significant differences between them: (1) the lack of reflection phases in the CCFs and (2) dominance of SPL and $SSPL$ waves in the CCFs. These differences originate in (1) the breakdown of equipartition among modes with different radial orders and (2) the dominance of shear-traction sources on the Earth's surface, respectively. Strong excitation of a PL wave by the shear-traction sources can explain the observed dominance of SPL and $SSPL$ waves. The cross-correlation analysis emphasizes efficiently excited modes such as surface waves and SPL and $SSPL$ waves. For further studies of body-wave exploration using seismic interferometry, we must consider these differences.

References

Aki, K. (1957), Space and time spectra of stationary stochastic waves, with special reference to microseisms, *Bull. Earthquake Res. Inst.*, *35*, 415–457.

Baag, C., and C. Langston (1985), Shear-coupled PL, *Geophys. J. R. Astron. Soc.*, *80*, 363–385.

Curtis, A., P. Gerstoft, H. Sato, R. Snieder, and K. Wapenaar (2006), Seismic interferometry turning noise into signal, *Leading Edge*, *25*, 1082–1092.

Dahlen, F., and J. Tromp (1998), *Theoretical Global Seismology*, 1025, Princeton University Press, Princeton.

Draganov, D., K. Wapenaar, W. Mulder, J. Singer, and A. Verdel (2007), Retrieval of reflections from seismic background-noise measurements, *Geophys. Res. Lett.*, *34*, L04305, doi: 10.1029/2006GL028735.

Dziewonski, A. M., and D. L. Anderson (1981), Preliminary reference Earth model, *Phys. Earth Planet. Inter.*, *25*, 297–356.

Ekström, G., M. Nettles, and A. M. Dziewoński (2012), The global CMT project 2004–2010: Centroid-moment tensors for 13,017 earthquakes, *Phys. Earth Planet. Inter.*, *200–201*, 1–9, doi:10.1016/j.pepi.2012.04.002.

Forghani, F., and R. Snieder (2010), Underestimation of body waves and feasibility of surface-wave reconstruction by seismic interferometry, *Leading Edge*, *29*, 790–794.

Nakahara, H. (2006), A systematic study of theoretical relations between spatial correlation and Green's function in one-, two- and three-dimensional random scalar wavefields, *Geophys. J. Int.*, *167*, 1097–1105. doi:10.1111/j.1365-246X.2006.03170.x.

Nishida, K., and N. Kobayashi (1999), Statistical features of Earth's continuous free oscillations, *J. Geophys. Res.*, *104*, 28,741–28,750.

Nishida, K., N. Kobayashi, and Y. Fukao (2002), Origin of Earth's ground noise from 2 to 20 mHz, *Geophys. Res. Lett.*, *29*, 10, 52-1–52-4

Nishida, K., H. Kawakatsu, and K. Obara (2008a), Three-dimensional crustal S wave velocity structure in Japan using microseismic data recorded by Hi-net tiltmeters, *J. Geophys. Res.*, *113*(B12), B10302, doi:10.1029/2007JB005395.

Nishida, K., H. Kawakatsu, Y. Fukao, and K. Obara (2008b), Background Love and Rayleigh waves simultaneously generated at the Pacific Ocean floors, *Geophys. Res. Lett.*, *35*, L16307, doi:10.1029/2008GL034753.

Nishida, K., J. P. Montagner, and H. Kawakatsu (2009), Global surface wave tomography using seismic hum, *Science*, *326*, 5949, 112.

Nishida, K. (2013), Earth's background free oscillations, *Annu. Rev. Earth Planet. Sci.*, *41,* accepted.

Oliver, J. (1961), On the long period character of shear waves, *Bull. Seismol. Soc. Am.*, *51*, 1, 1–12.

Peterson, J. (1993), Observations and modeling of seismic background noise, *U.S. Geol. Surv. Open File Rep.*, *93-322*, 1.

Poli, P., H. A. Pedersen, M. Campillo, and POLENET LAPNET working group (2012a), Emergence of body waves from cross-correlation of seismic noise, *Geophys. J. Int*, *188*, 549–558.

Poli, P., M. Campillo, H. A. Pedersen, and LAPNET working group (2012b), Body-wave imaging of Earth's mantle discontinuities from ambient Seismic noise, *Science*, *338*, 6110, 1063–1065, doi:10.1126/science.1228194.

Ritzwoller, M. H., F. C. Lin, and W. Shen (2011), Ambient noise tomography with a large seismic array, *C. R. Geosci.*, 13 pages, doi:10.1016/j.crte.2011.03.007.

Roux, P., P-waves from cross-correlation of seismic noise (2005), *Geophys. Res. Lett.*, *32*, L19303, doi:10.1029/2005GL023803.

Shapiro, N. M., M. Campillo, L. Stehly, and M. H. Ritzwoller (2005), High-resolution surface-wave tomography from ambient seismic noise, *Science, 307*, 5715, 1615–1518.

Shearer, P.M., and T.G. Masters (1992), Global mapping of topography on the 660 km discontinuity, *Nature, 355*, 791–796.

Snieder, R. (2004), Extracting the Green's function from the correlation of coda waves: A derivation based on stationary phase. *Phys. Rev. E*, *69*, 046610, doi:10.1103/PhysRevE.66.046610.

Snieder, R., Y. Fan, E. Slob, and K. Wapenaar (2010), Equipartitioning is not sufficient for Green's function extraction, *Earthquake Sci., 23*, 403–415.

Tonegawa, T., K. Nishida, T. Watanabe, and K. Shiomi (2009), Seismic interferometry of teleseismic S-wave coda for retrieval of body waves: An application to the Philippine Sea slab underneath the Japanese Islands, *Geophys. J. Int., 178*, 1574–1586.

Earthquake Research Institute, University of Tokyo, 1-1-1 Yayoi 1, Bunkyo-ku, Tokyo 113-0032, Japan (knishida@eri.u-tokyo.ac.jp)
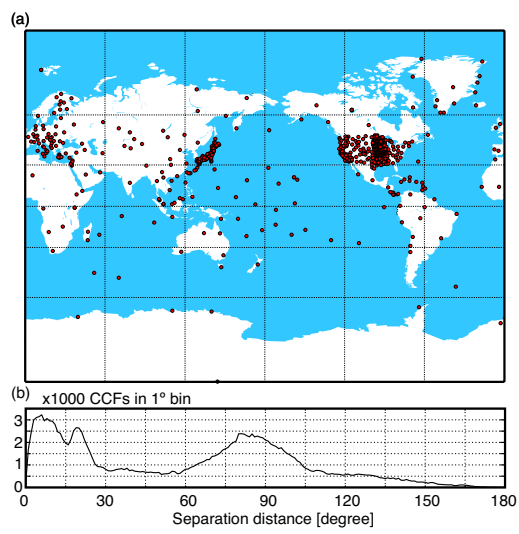
Figure 1. (a) Location map of 658 stations used in this study (red circles). (b) A histogram showing the distribution of receiver-receiver ranges for the CCFs used in this paper. The number in 1° range bins are plotted as a function of range.
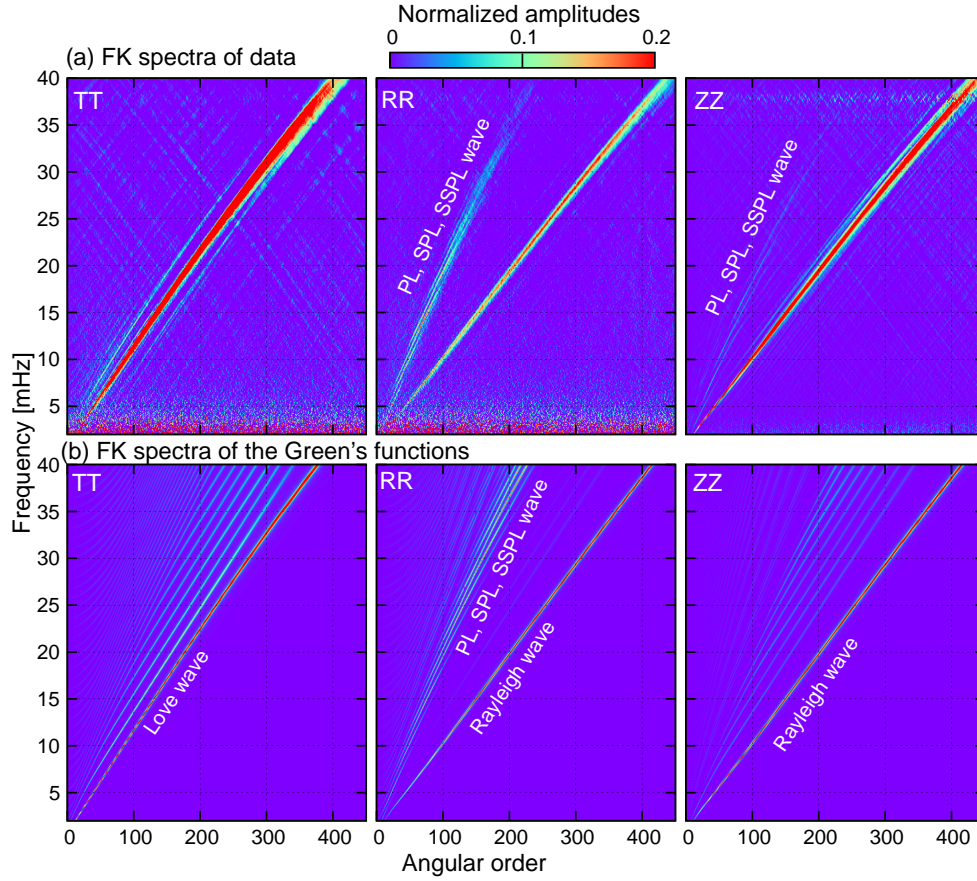
Figure 2. (a) FK spectra of seismic hum. The left panel shows the TT component, the middle one shows the RR component, and the right one shows the ZZ component. The horizontal axes show angular order, and the vertical ones show the frequency in milli Hertz [mHz]. Their color shows PSDs normalized by NLNM. Noise levels of the horizontal components (RR and TT) at low frequency are higher than that of the vertical one (ZZ). (b) FK spectra of corresponding components of the Green's functions. Also shown are names of some typical associated seismic phases.
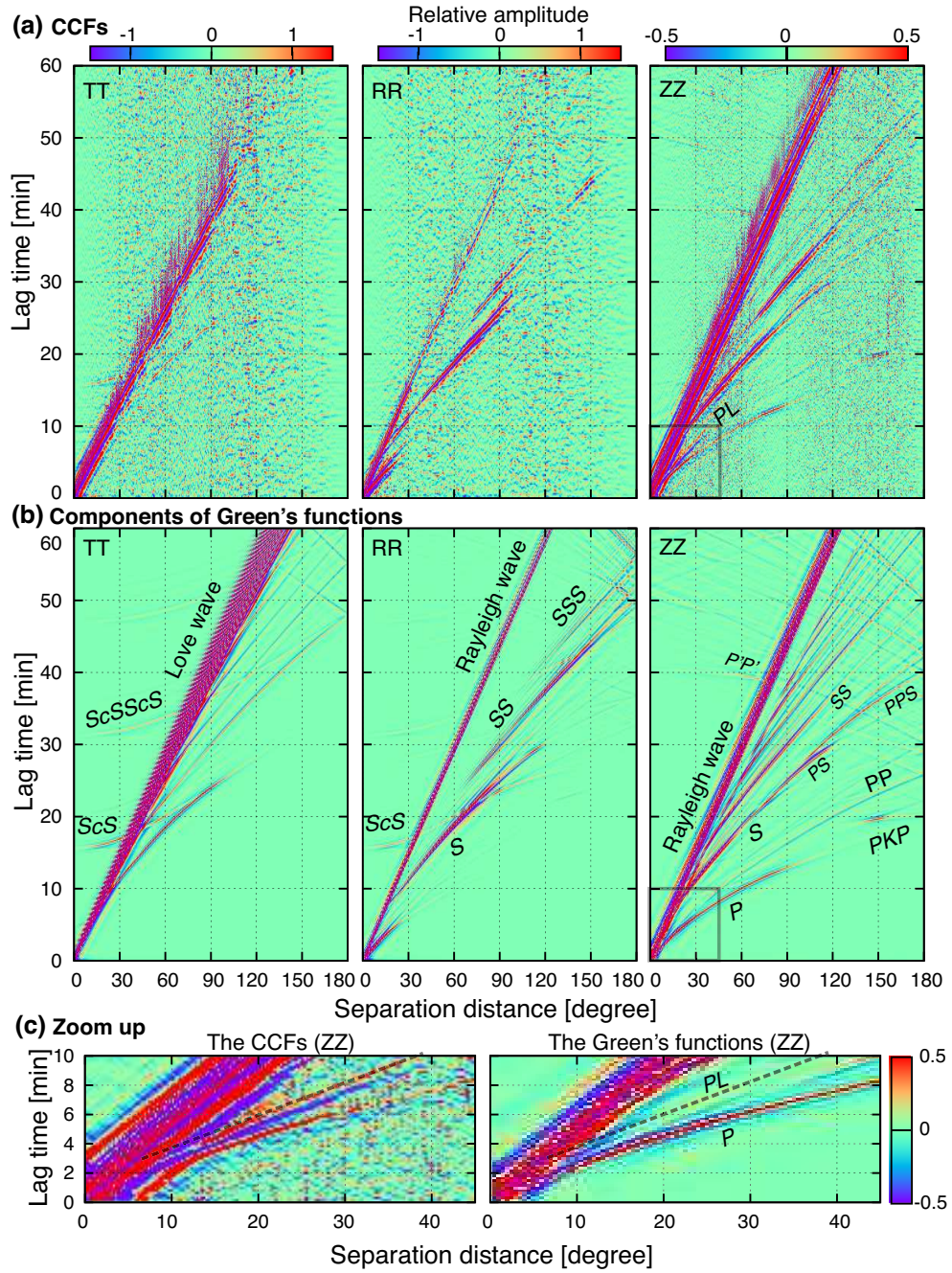
Figure 3. (a) Record sections of TT, RR, and ZZ components of CCFs. The horizontal axes show separation distance between station pairs, and the vertical axes show the lag time in minutes. (b) TT, RR, and ZZ components of the Green's functions. Also shown are names of some typical seismic phases. (c) Zoom up of the two rectangular areas in the ZZ component. Also shown are P and SPL waves.
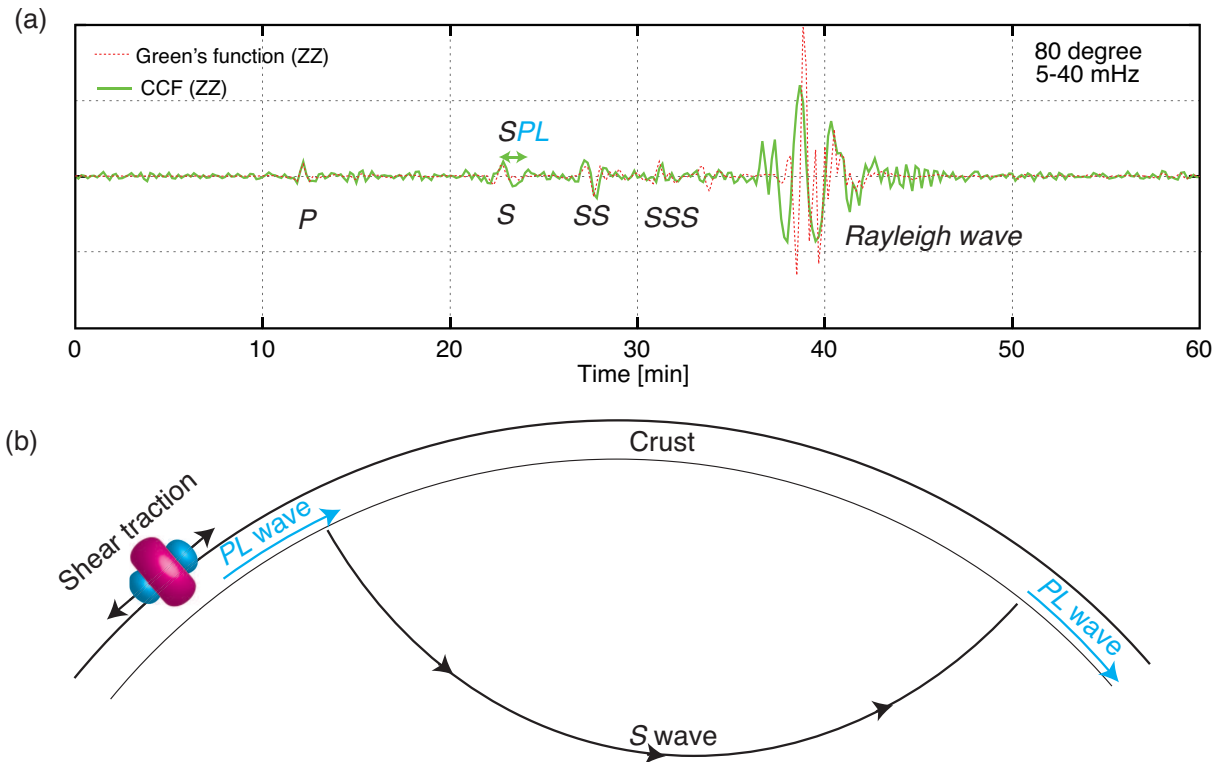
Figure 4. (a) Comparison of ZZ component of the CCF at $80°$ with the corresponding component of the Green's function. (b) Schematic figure of the coupling mechanism between S and PL waves, and the radiation pattern from the shear-traction source. The red color shows the radiation pattern of an S wave, and the blue color shows that of a P wave.